

# Effect of Brass Interlayer Sheet on Microstructure and Joint Performance of Ultrasonic Spot-Welded Copper-Steel Joints

Mantra Prasad Satpathy, Abhishek Kumar, and Susanta Kumar Sahoo

(Submitted September 28, 2016; in revised form May 4, 2017; published online June 13, 2017)

Solid-state ultrasonic spot welding (USW) inevitably offers a potential solution for joining dissimilar metal combination like copper (Cu) and steel (SS). In this study, the USW has been performed on Cu (UNS C10100) and SS (AISI 304) with brass interlayer by varying various welding parameters, aiming to identify the interfacial reaction, changes in microstructure and weld strength. The highest tensile shear and T-peel failure loads of 1277 and 174 N are achieved at the optimum conditions like 68  $\mu\text{m}$  of vibration amplitude, 0.42 MPa of weld pressure and 1 s of weld time. The fractured surface analysis of brass interlayer and AISI 304 stainless steel samples reveals the features like swirls, voids and intermetallic compounds (IMCs). These IMCs are composed of CuZn and FeZn composite-like structures with  $\sim 1.0 \mu\text{m}$  thickness. This confirms that the weld quality is specifically sensitive to the levels of input parameter combinations as well as the type of material present on the sonotrode side.

**Keywords** brass interlayer, intermetallic compounds, tensile shear strength, T-peel strength, ultrasonic metal welding, weld quality

## 1. Introduction

During the past few years, there is a drastic increase in demand of dissimilar metal welding, especially in the automobile sector by providing lightweight solutions (Ref 1). Moreover, the welding of thin and dissimilar metal sheets is a robust and complicated process and it cannot be easily achieved by the fusion welding process. Because these sheets are readily get melted without proper fusion, producing a large heat-affected zone (HAZ). In addition to it, some predominant features like porosity, voids, distortion and intermetallic compounds (IMCs) are also formed, which are the primary causes for lowering the strength of the weld (Ref 2). However, with the advent of increasing other welding techniques like resistance spot welding (RSW), friction stir welding (FSW) and ultrasonic welding (USW), these difficulties can be avoided. Although RSW is most popular in this field, one primary concern is the consumption of energy during the welding process. It consumes almost 10% of more energy than USW (Ref 3). Likewise, the long welding cycle and severe working condition at joint limits the application of FSW (Ref 4). USW includes the rubbing of metal sheets with high-frequency vibration to break the oxide layer, and microwelds are formed due to localized heating at the interface (Ref 5). Thus, it is considered to be one of the emerging and popular techniques in the solid-state welding

field for joining nonferrous and ferrous metals with consumption of least energy (Ref 6).

The copper-stainless steel (AISI 304) are extensively used in power generation, chemical equipment and utensil industries because of their excellent thermal conductivity as well as strength. There are also many reports published by various researchers on the fusion welding of copper to AISI 304. Magnabosco et al. (Ref 7) used electron beam welding to weld copper with austenitic stainless steel plates and studied the fusion zone microstructures. The results showed the defects such as porosity and microfissures due to poor mixing of the materials. Likewise, Mai and Spowage (Ref 8) performed experiments on copper-steel butt joints produced by laser welding. It was found that most of the energy was absorbed by steel, and limited copper was dissolved due to differences in their chemical properties. Meanwhile, Phanikumar (Ref 9) attempted to join Cu-Fe using a CO<sub>2</sub> laser and the microstructures found on the copper side were very rough and of curved type. However, less number of research papers are available for solid-state joining of copper and steel. Durgutlu et al. (Ref 10) carried out explosive welding experiments on copper and steel sheets and confirmed that these metals could be joined effectively without the formation of IMCs. Furthermore, the work reported by Imani et al. (Ref 11) on the friction stir welding of Cu to SS304L showed that minimal amount of cracks and IMCs were formed with 30% less ultimate tensile strength of the copper metal. Shiri et al. (Ref 12) also conducted tests to join SS304 with copper using gas tungsten arc welding with various filler materials. The results showed the 96% of weld strength could be achieved with a higher hardness at the fusion zone. One of the biggest problem while joining copper with steel is that copper has higher thermal conductivity than SS304 (Ref 13), and thus, it is responsible for the rapid cooling of copper and formation of cracks in the weldment.

It is well known that the chemical compositions and various properties of weldments play a vital role in producing IMCs in dissimilar welding. Previous researchers like Zhao et al. (Ref

Mantra Prasad Satpathy, Department of Mechanical Engineering, ITS, IFHE, Hyderabad 501203, India; and Abhishek Kumar and Susanta Kumar Sahoo, Department of Mechanical Engineering, National Institute of Technology Rourkela, Odisha 769008, India. Contact e-mail: mantraofficial@gmail.com.

14), Balasundaram et al. (Ref 15) and Wang et al. (Ref 16) also observed these brittle IMCs were the primary reasons for the joint failure. However, they did not address any means to improve the joint. Moreover, some of the previous studies also demonstrated about the welding of copper and steel, but to the author's knowledge, there are no systematic studies present in the open literature to describe the effect of brass interlayer on the enhancement of mechanical performance and quality of the joints. Brass was selected because its Zn constituent has the ability to interact well with the copper at elevated temperature as given by Cu-Zn binary phase diagram (Ref 17). Thus, Zn can inhibit the formation of brittle IMCs between Cu and Fe

resulting high weld strength. Thus, the present study describes the effect of brass interlayer sheets and the type of stacking of metal sheets on the weld strength. To reveal the quality of Cu-AISI 304 stainless steel joints made by USW, particular emphasis has been given to the microstructural analysis and its related mechanical properties.

## 2. Materials and Experimental Details

The workpiece materials used in this study were commercially available 0.4-mm-thick pure copper (99.99% Cu) and 0.2-mm-thick AISI 304 stainless steel (69%Fe-9.20%Ni-18%Cr-2.65%Mn-1%Si-0.08%C-0.04%P-0.03%S) sheets. Meantime, the brass (UNS C27000) (63%Cu-0.070%Fe-36.83%Zn-0.10%Pb) sheet of thickness 0.1 mm was considered as the interlayer. Table 1 lists the physical and mechanical properties of the interlayer. After conducting a lot of trial experiments, the dimensions of the weld coupons were selected as 80 mm long  $\times$  20 mm wide so that these were vibrated in a resonance condition. Meantime, the surfaces were cleaned with acetone to remove impurities and contaminants present on it. All the welds were produced by a lateral drive ultrasonic metal welder (Telsonic® M4000) (Fig. 1) with a 20-mm overlap. Thus, the dimensions of the interlayer sheets were also selected as 20 mm  $\times$  20 mm (Fig. 2). The welding system was operated

**Table 1** Physical, mechanical and thermal properties of interlayer

Properties	Unit	UNS C27000
Density	kg/m <sup>3</sup>	8470
Young's modulus	Pa	105E9
Poisson's ratio		0.3
Ultimate tensile strength	Pa	420.4E6
Yield strength	Pa	336.1E6
Coefficient of thermal expansion	°C <sup>-1</sup>	20.3E-6
Thermal conductivity	W/m °C	116
Specific heat	J/kg °C	380
Melting point	°C	930

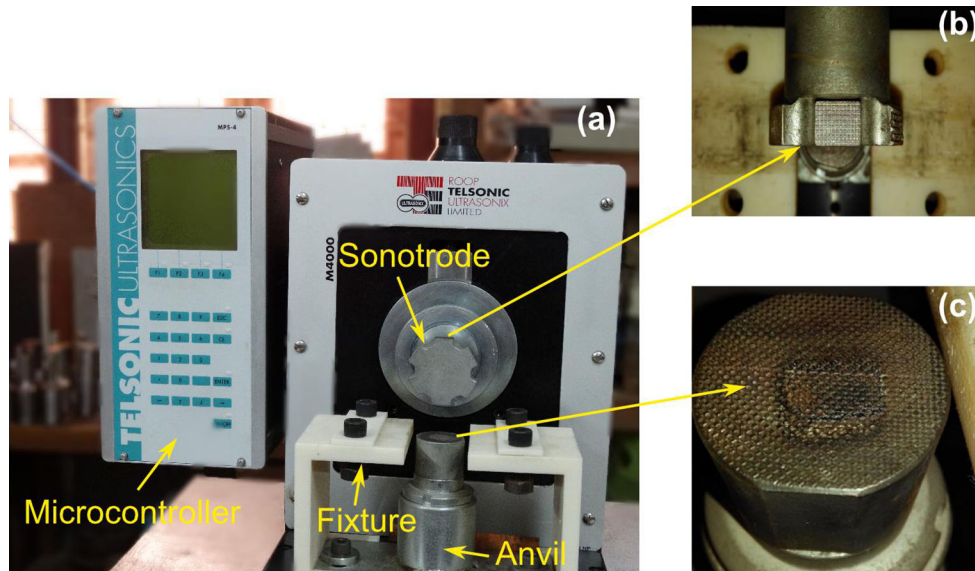


**Fig. 1** Ultrasonic metal welder: (a) high-power welding press; (b) enlarged knurled sonotrode; (c) enlarged knurled anvil

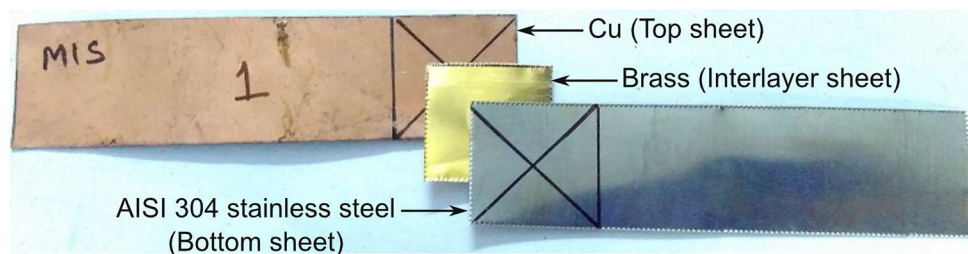


**Fig. 2** Welding coupons with interlayer sheet

at 20 kHz frequency with 3 kW of maximum output power. The joints were produced in time control mode by varying various process parameters such as vibration amplitude, weld time and weld pressure. In the present analysis, the experiments have been performed in two phases. The first phase of investigation included the selection of weld coupon combination based on its orientation. Thus, three levels of each input parameter selected based upon the number of trial experiments, and the L9 orthogonal array was employed to carry out the tests. The particular experimental domain is presented in Table 2. According to this table, each nine numbers of samples have been selected for tensile shear and T-peel tests. Meanwhile, the second phase of investigation on the selected combination further performed, and the full factorial design of experiment with six replications (i.e., based on Table 2) was adopted for the in detailed analysis of the various features of welded joints. In this context, a total of 162 numbers of samples were prepared and out of that half of the samples are selected for tensile shear test and rest for the T-peel test. In order to evaluate the soundness of the joints, the tensile shear and T-peel tests were performed for each weld condition by using a universal testing machine (INSTRON® 1195) with a constant crosshead speed of 2 mm/min. The schematic diagram of weld coupon configuration used for these two tests is presented in Fig. 3. Furthermore, microstructural examinations of “under,” “good” and “over” weld samples were executed by optical microscopy and scanning electron microscopy (SEM) (JEOL® JSM-6084LV) with energy dispersive spectroscopy (EDS). These metallographic samples were cut from the weld cross section, mounted and etched for the precise observation. Phase

identification on both the fractured surfaces of copper and stainless steel sides was revealed by Bruker® D8ADVANCE x-ray diffractometer (XRD) with cobalt receptor. The diffraction angle ( $2\theta$ ) varied from  $30^\circ$  to  $110^\circ$  with a step size of  $2^\circ$  per minute.

### 3. Results and Discussion

#### 3.1 Tensile Shear and T-peel Failure Loads

The maximum tensile shear failure loads for the first phase of experiment are represented in Fig. 4. For each weld condition, it is clearly noticed from the illustration that when the Cu is on the sonotrode side (i.e., top position), then the joint strength is significantly higher than the case in which AISI 304 stainless steel is on the top position. The primary reason for this kind of phenomenon is that Cu is softer as comparable to AISI 304. Thus, Cu is more amenable to plastic deformation due to the generation of high temperature, and thereby it diffuses into steel for achieving a sound joint. Hence, the second phase of experiments has been conducted by keeping Cu on the sonotrode side AISI 304 on the anvil side with brass as interlayer material. The plots of tensile shear and T-peel failure loads with the variation of weld pressure and weld time parameters at different vibration amplitudes are shown in Fig. 5 and 6. The failure load profiles for all the vibration amplitudes showed a similar pattern, in which tensile shear and T-peel failure loads increased with rising in weld time up to 1 s and then decreased with further increased in weld time. With support for this type of profile nature, Lee et al. (Ref 18) and Zhang et al. (Ref 19, 20) also observed the growth of U-tensile load up to 0.6 s of weld time, and then it decreased. It has been established that at lower weld time, less amount of ultrasonic energy was supplied to the faying surface, and thus, the temperature developed at the interface was not high enough to soften the materials (Ref 21). But with the increase in weld time, weld pressure and vibration amplitude, both tensile shear and T-peel failure loads increased due to the formation of high interface temperature and enhanced strain rate. Thus, it results

**Table 2 Domain of experiments adopted for USMW of dissimilar thickness Cu-AISI 304 weld coupons**

Factors	Level 1	Level 2	Level 3
Amplitude, $\mu\text{m}$	54	60	68
Weld pressure, MPa	0.38	0.42	0.46
Weld time, s	0.8	1.0	1.2

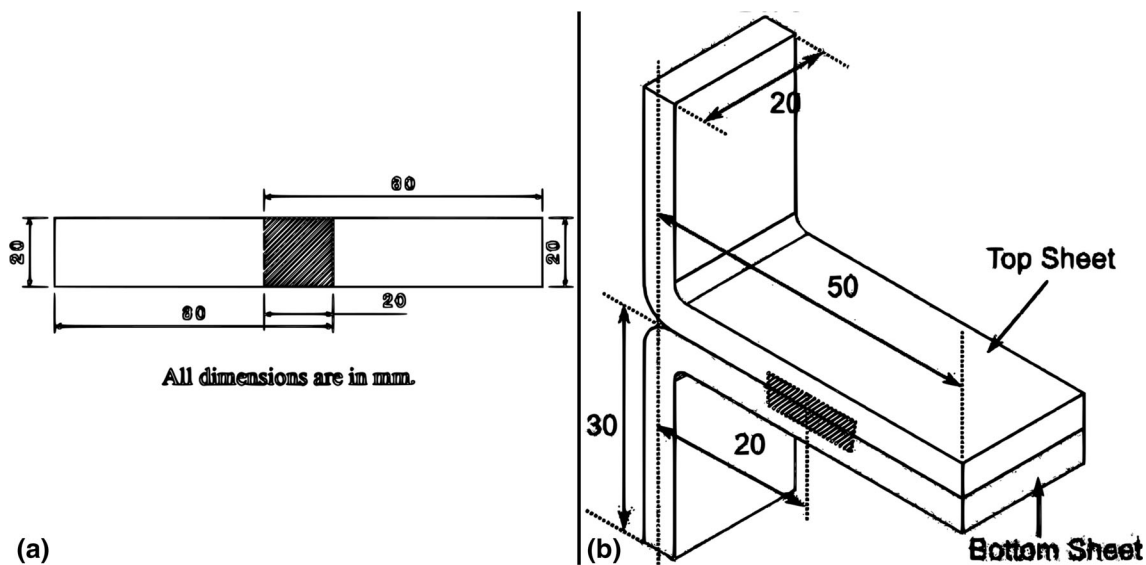


**Fig. 3** Schematic diagram of weld coupons used for (a) tensile shear and (b) T-peel tests

in higher diffusion rate between Cu and AISI 304 stainless steel. The maximum tensile shear failure load of 1277 N and T-peel strength of 174 N are observed at weld pressure of 0.42 MPa, weld time of 1 s and 68  $\mu\text{m}$  of vibration amplitude. The most noticeable feature observed in this setting was the

ductile nature of Cu sheets due to insertion of the brass interlayer. During the tensile test, the welded joint exhibited higher shear stress than the ultimate tensile strength of Cu. Thus, the base metal Cu stretched more and broke outside the weld spot. In other words, it can be said that the load bearing capacity of the weld spot is higher than the copper metal. Furthermore, when the weld time and weld pressure increased beyond these parameter values, then the top Cu metal severely deformed and microcracks were generated at the edge of the nugget zone with a thicker IMC. Similar results also have been reported in some literature (Ref 22-26).

### 3.2 Weld Interface Microstructure

In this section, the detailed description of weld quality and its correlation with joint attributes is presented at various weld conditions. Figure 7 represents the optical micrographs of Cu-AISI 304 stainless steel weld cross sections at various input parameter values. It can be observed from Fig. 7(a) that there exist distinct gaps between the sheets and it is referred as the “under weld” condition. Moreover, this condition occurred at the lowest value of each parameter, and thus less amount of ultrasonic energy is transferred to the faying zone. Similarly, as the values of the input parameters increased, the delivery of ultrasonic energy to the faying surface also increased. Therefore, the metallurgical bonds happened at multiple regions with a uniform grain structure along the weld cross section. Figure 7(b)

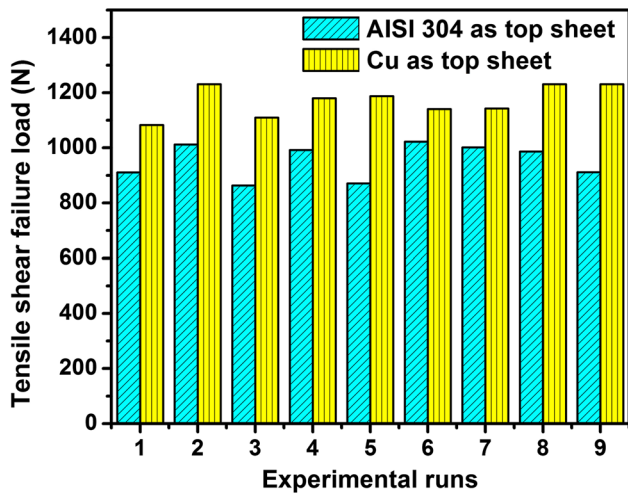


Fig. 4 Comparison of tensile shear test results for first phase of experiment between Cu and AISI 304 stainless steel sheets

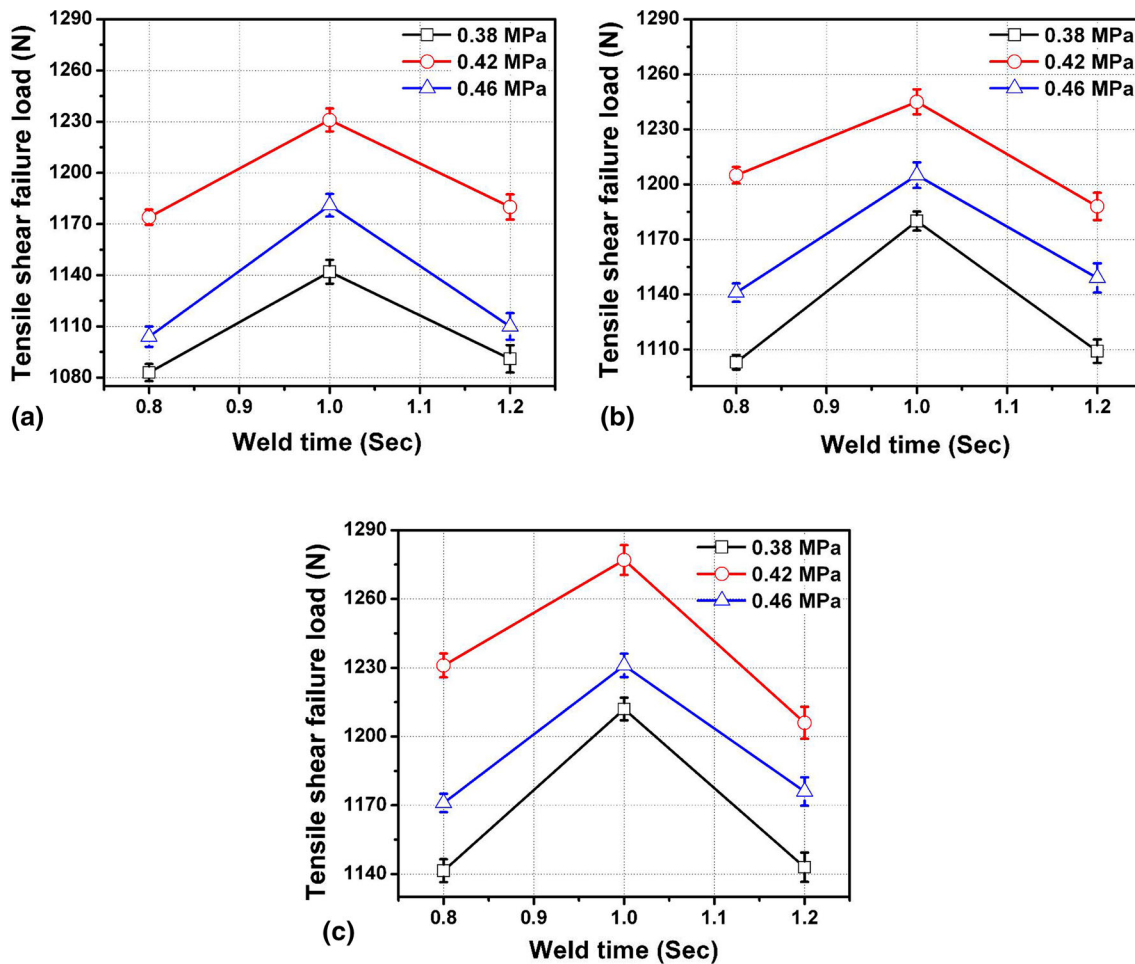


Fig. 5 Tensile shear failure loads of USWed Cu-AISI 304 stainless steel joints at different vibration amplitudes

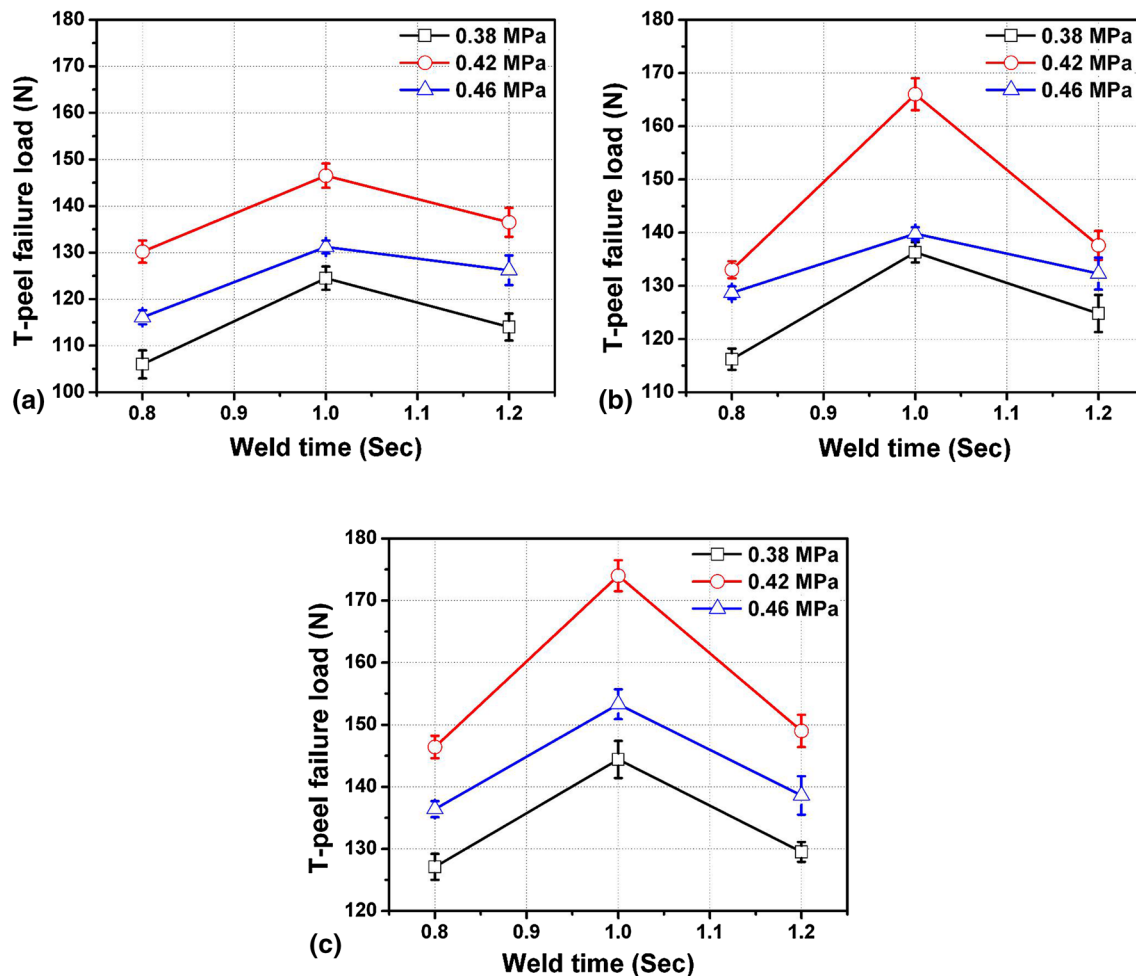


Fig. 6 T-peel failure loads of USWed Cu-AISI 304 stainless steel joints at different vibration amplitudes

shows this condition, and it is referred as “good weld” condition with the maximum tensile shear failure load of 1277 N and a T-peel load of 174 N. There were also mechanical interlocking and swirl-like features noticed throughout the bond line which could provide extra bonding strength to the joint. The swirling phenomenon at the weld interface was due to the penetration of sonotrode knurls into the workpiece at higher ultrasonic energy. Thus, the extreme wavy-type interface was observed under the sonotrode knurls, and the wave peaks formed fold-like feature in a certain zone. This swirling deformation exhibits the rise of tensile shear and T-peel failure loads due to localized mechanical interlocking in the weld zone. However, the density of metallic bonds and the interlocking feature were larger in the case of “over weld” samples than “good weld.” But due to severe plastic deformation of the weld materials, the microcracks were noticed (Fig. 7c) and subsequently the tensile shear and T-peel failure loads decreased. These microcracks were typically formed on the Cu side. It can be inferred from this image that the molten Zn component of brass is squeezed out from the weld surface and breach to the Cu surface through intergranular cracks. The possible reason for these intergranular cracks is due to the liquid metal embrittlement (LME) phenomenon where the ductile materials became brittle while in contact with the liquid metal (Ref 27). Bruscato (Ref 28) also demonstrated that LME caused a destructive crack in the stainless steel when the molten Zn was in contact with it. This over weld condition was observed at 68  $\mu\text{m}$  of vibration amplitude, 0.46 MPa of weld pressure and 1.2 s of

weld time. Moreover, to analyze the weld attributes more precisely and diligently, higher magnification backscattered SEM images at the weld interface for various weld conditions are shown in Fig. 8. Figure 8(a) demonstrates the under weld condition where voids are clearly noticed. As spotted from Fig. 8(b) and (c), the good welding and over welding conditions displayed improve bond quality due to interface stirring. However, microcracks were noticed in the case of over weld samples. As described before, the higher weld energy produces more amount of interface temperature. Thus, it softens the material, and the sonotrode tips penetrate more into the sheets producing massive plastic deformation. These types of features were also supported by many researchers (Ref 29, 30).

### 3.3 Energy Dispersive Spectroscopy (EDS)

The EDS line scan analysis was performed in order to verify the possible phase formations on the weld cross sections of good weld samples, and it is shown in Fig. 9. From previous studies, it was evident that the interface layer was composed of IMCs through interatomic diffusion (Ref 31). Figure 9(a) reveals a magnified portion of the weld cross section where the heterogeneous regions are marked as A, B and C points. The chemical composition at point A (white region) was verified from EDS point scan analysis, and it was (in at.%) 51.23Cu-27.80Zn-10.34Fe-7.41Ni-3.22Cr, which suggests that as this layer is just below the Cu specimen, the effect of it on

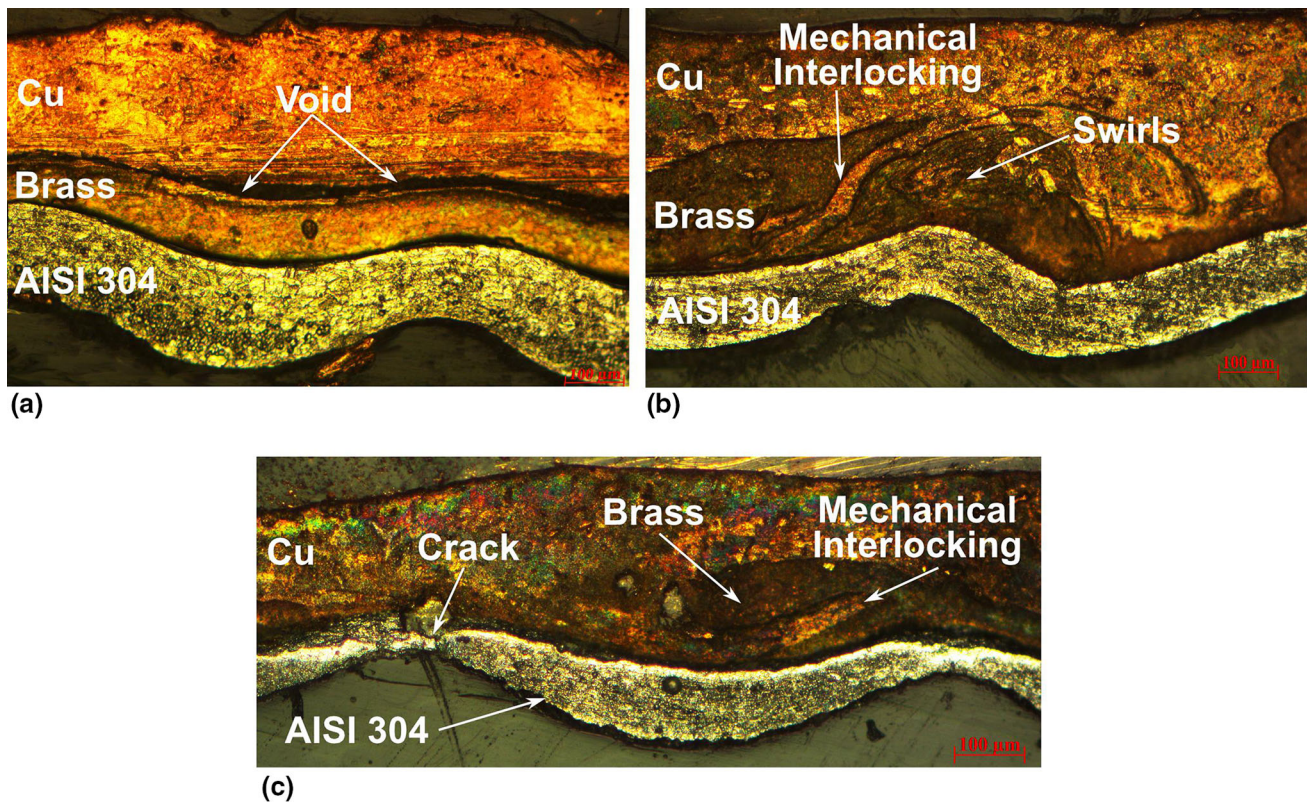


**Fig. 7** Optical micrographs of USWed Cu-AISI 304 stainless steel weld cross sections at various welding conditions

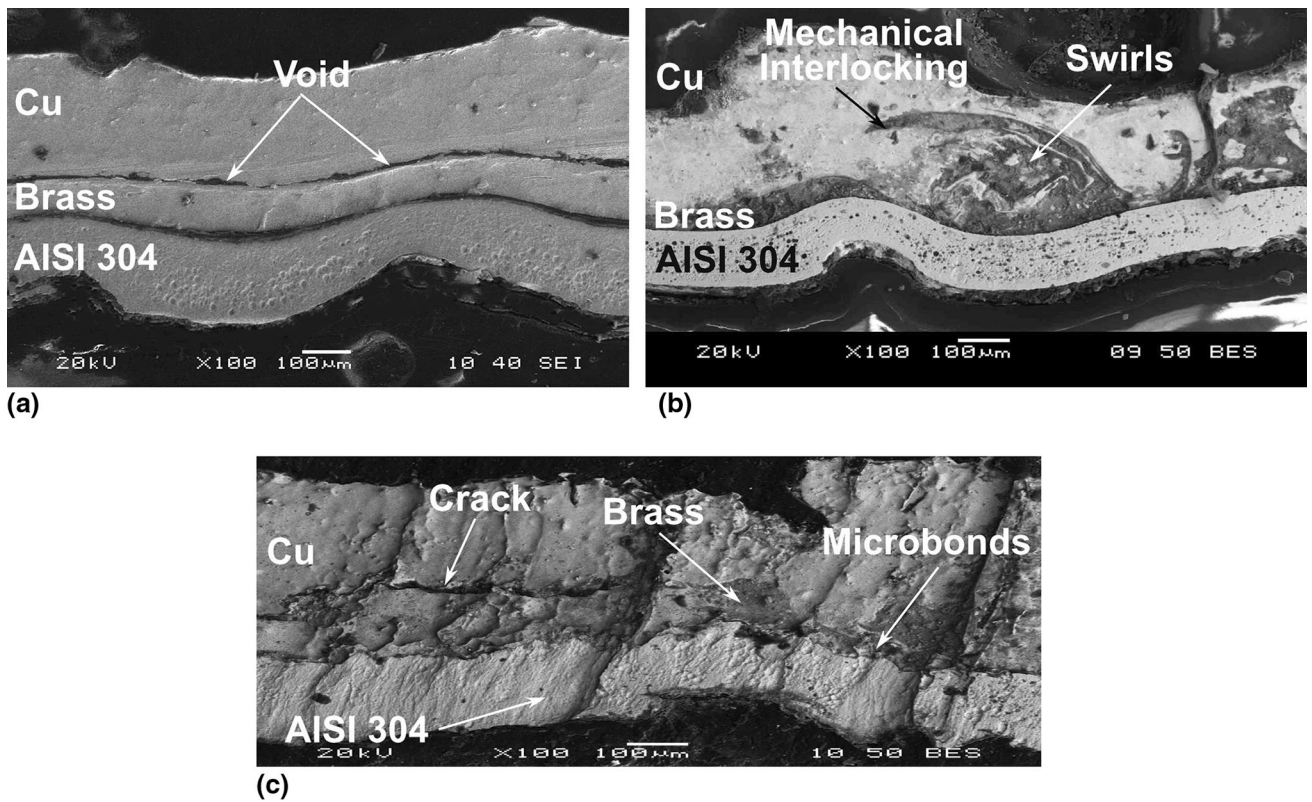


**Fig. 8** SEM images at the weld cross sections of USWed Cu-AISI 304 stainless steel joints for various welding conditions

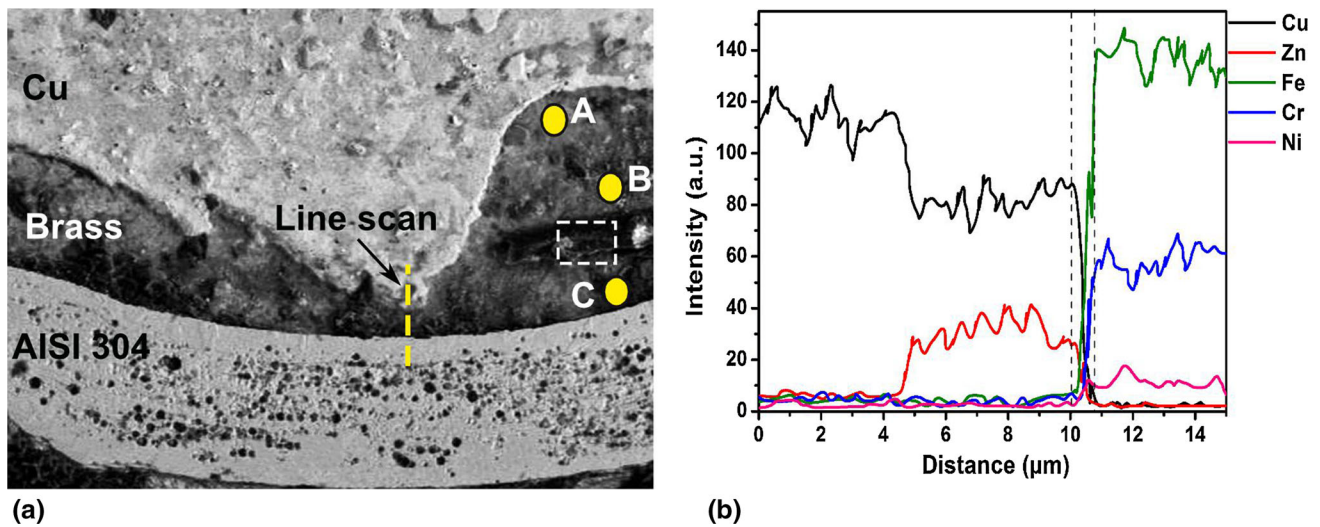


**Fig. 9** Highly magnified backscattered SEM image with EDS line scan at the weld cross section of USWed Cu-AISI 304 stainless steel joint and the corresponding result for good weld condition

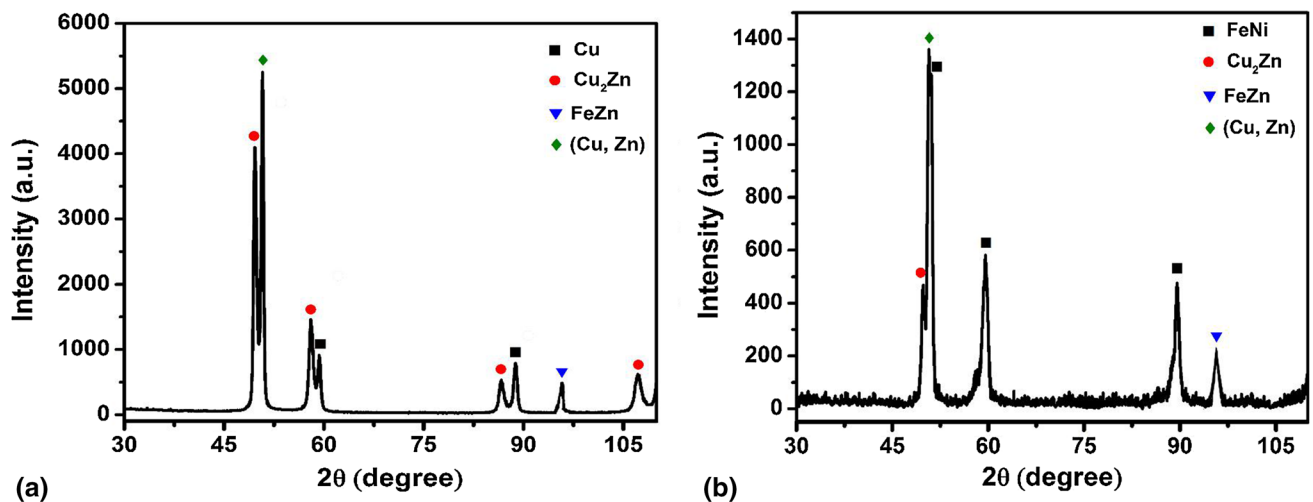


**Fig. 10** XRD scan results acquired from on fractured surfaces of brass and AISI 304 side for good weld condition

the IMC is more. Likewise, the EDS point analysis on the gray (point B) and black region (point C) indicates a chemical composition of (in at.%) 24.52Cu-45.83Zn-13.69Fe-9.83Ni-4.13Cr and 12.02Cu-38.29Zn-33.64Fe-11.23Ni-4.82Cr, respectively, noticeably signifying that the intermetallic layer is enriched with Cu, Zn, Fe, Ni and Cr elements. The white dotted box in this region presents a spiral type of feature which belongs to Fe-Zn as evident by the high content of Fe and Zn. Normally, due to the lower melting point of Cu and brass materials, the solid solution of the atoms of these metals get diffused to Fe lattice because of their high energetic nature. From the Cu-AISI 304 line scan analysis (Fig. 9b), it can be inferred that at a distance of  $\sim 10 \mu\text{m}$ , the Cu concentration is starting to decrease. Similarly, at the beginning of the line scan analysis, there is a negligible amount of Zn is present. But toward the weld interface, the amount of Zn gradually increases and then it also decreases around a distance of  $\sim 10 \mu\text{m}$ . According to the binary phase diagram of Cu and Zn (Ref 17) and Cu and Fe (Ref 32), some brittle intermetallic compounds such as CuZn and FeZn could be formed, which were confirmed later by x-ray diffraction analysis. Thus, due to the

formation of these unwanted brittle IMC phases during the welding of Cu-AISI 304, the fracture happened, and the strength of the joint was lowered.

### 3.4 X-ray Diffractions

To confirm the phases identified by EDS analysis, the x-ray diffraction (XRD) scans (Fig. 10) were performed on the fractured surfaces of the good weld samples of brass and stainless steel sheets after the T-peel test. Moreover, during the T-peel test, it was observed that interfacial failure happened at the UNS C27000 brass-AISI 304 stainless steel interface. Thus, it depicts that the metallurgical bonds formed between UNS C27000-AISI 304 are weaker than the Cu-UNS C27000 interface. Meantime, the solubility of Cu in Fe is very low. Hence, no IMC is expected between Fe and Cu. But Fe-Zn and Cu-Zn compounds can be expected as they form IMCs at these welding conditions. Figure 10(a) represents the XRD analysis on the brass side. It is clear that the sharp peaks have been occupied by  $\text{Cu}_2\text{Zn}$ , CuZn and Cu with some of the peaks of FeZn compounds. Furthermore, on the fracture side of AISI 304 (Fig. 10b), elements such as

CuZn and FeZn are noticed along with Cu<sub>2</sub>Zn and FeNi. The root cause of formation of these compounds is unknown, and some hypothesis can be rendered. Firstly, due to insertion of brass as interlayer sheet, the friction between the samples increases and thus the diffusion rate of metals also increases. Secondly, Zn may act as a catalyst during the interface reaction between Cu and AISI 304 weld samples. Cu<sub>2</sub>Zn and FeZn peaks suggest that some Zn reacted with Cu and Fe to produce these compounds. These results from the XRD analysis confer that the mechanical performance of the joint significantly depends on the formation of brittle IMCs. However, more research needs to be carried out in order to reveal and understand the interface reaction of Zn with Cu and AISI 304.

## 4. Conclusions

Ultrasonic spot welding was successfully used to join Cu with AISI 304 stainless steel using a brass interlayer placed between the sheets. The mechanical performances of different quality welds were investigated, and the relationship between those performances with the weld attributes was qualitatively identified. The major conclusions of the present study are as follows:

- (1) The order of stacking of weld coupons affects the joint strength. Cu on the sonotrode side shows higher tensile shear failure load than AISI 304 stainless steel for each weld condition. The highest tensile shear failure load of 1277 N and T-peel failure load of 174 N achieved at 68 μm of vibration amplitude, 0.42 MPa of weld pressure and 1 s of weld time. This high bonding strength is due to the metallurgical bonding and mechanical interlocking.
- (2) Microstructural analysis revealed that there are three different kinds of weld quality (i.e., under, good and over weld) present depending upon the amount of ultrasonic energy transmitted to the joint area. As the good weld samples have more bond density at the interface layer; thus, it shows the highest weld strength. Meantime, for the over weld specimens, material flow and extensive plastic deformation of Cu occurs at the interface. Thus, microcracks are generated around the weld spot.
- (3) Although the USW has short weld cycle, the thickness of IMC layer grows with the increase in the levels of input parameters. It is confirmed from EDS line scan analysis that the ~1-μm-thick, brittle IMC compound is the primary reason for conciliating the soundness of the joint.
- (4) XRD analysis also revealed that FeZn phase was mainly present on both the fractured surfaces along with CuZn phase during the welding of Cu to AISI 304 stainless steel joints.

The Scientific understanding of this study can guide the welders to achieve a high-quality joint within a particular process parameter region.

## References

1. P. Prangnell, F. Haddadi, and Y.C. Chen, Ultrasonic Spot Welding of Aluminium to Steel for Automotive Applications-Microstructure and Optimisation, *Mater. Sci. Technol.*, 2011, **27**(3), p 617–624
2. I. Galvao, R.M. Leal, A. Loureiro, and D.M. Rodrigues, Material Flow in Heterogeneous Friction Stir Welding of Aluminium and Copper Thin Sheets, *Sci. Technol. Weld. Join.*, 2013, **15**(8), p 654–660
3. P.B. Prangnell and D. Bakavos, Novel Approaches to Friction Spot Welding Thin Aluminium Automotive Sheet, *Mater. Sci. Forum*, 2010, **638**, p 1237–1242
4. V.K. Patel, S.D. Bhole, and D.L. Chen, Ultrasonic Spot Welded AZ31 Magnesium Alloy: Microstructure, Texture, and Lap Shear Strength, *Mater. Sci. Eng. A*, 2013, **569**, p 78–85
5. M. Annoni and M. Carboni, Ultrasonic Metal Welding of AA 6022–T4 Lap Joints: Part I—Technological Characterisation and Static Mechanical Behaviour, *Sci. Technol. Weld. Join.*, 2011, **16**(2), p 107–115
6. S. Matsuoka and H. Imai, Direct Welding of Different Metals Used Ultrasonic Vibration, *J. Mater. Process. Technol.*, 2009, **209**(2), p 954–960
7. I. Magnabosco, P. Ferro, F. Bonollo, and L. Arnberg, An Investigation of Fusion Zone Microstructures in Electron Beam Welding of Copper–Stainless Steel, *Mater. Sci. Eng. A*, 2006, **424**(1), p 163–173
8. T.A. Mai and A.C. Spowage, Characterisation of Dissimilar Joints in Laser Welding of Steel-Kovar, Copper-Steel and Copper-Aluminium, *Mater. Sci. Eng. A*, 2004, **374**(1), p 224–233
9. G. Phanikumar, S. Manjini, P. Dutta, K. Chattopadhyay, and J. Mazumder, Characterization of a Continuous CO<sub>2</sub> Laser-Welded Fe-Cu Dissimilar Couple, *Metall. Mater. Trans. A*, 2005, **36**(8), p 2137–2147
10. A. Durgutlu, B. Gülenç, and F. Findik, Examination of Copper/Stainless Steel Joints Formed by Explosive Welding, *Mater. Des.*, 2005, **26**(6), p 497–507
11. Y. Imani, M.K. Givi, and M. Guillot, Improving Friction Stir Welding Between Copper and 304L Stainless Steel, *Adv. Mater. Res.*, 2012, **409**, p 263–268
12. S.G. Shiri, M. Nazarzadeh, M. Sharifitabar, and M.S. Afarani, Gas Tungsten Arc Welding of CP-Copper to 304 Stainless Steel Using Different Filler Materials, *Trans. Nonferrous Met. Soc. China*, 2012, **22**(12), p 2937–2942
13. J.D. Destefani, Properties and Selection: Nonferrous Alloys and Special-Purpose Materials, *ASM Handb.*, 1992, **2**, p 1770
14. Y.Y. Zhao, D. Li, and Y.S. Zhang, Effect of Welding Energy on Interface Zone of Al-Cu Ultrasonic Welded Joint, *Sci. Technol. Weld. Join.*, 2013, **18**(4), p 354–360
15. R. Balasundaram, V.K. Patel, S.D. Bhole, and D.L. Chen, Effect of Zinc Interlayer on Ultrasonic Spot Welded Aluminum-to-Copper Joints, *Mater. Sci. Eng. A*, 2014, **607**, p 277–286
16. S.Q. Wang, V.K. Patel, S.D. Bhole, G.D. Wen, and D.L. Chen, Microstructure and Mechanical Properties of Ultrasonic Spot Welded Al/Ti Alloy Joints, *Mater. Des.*, 2015, **78**, p 33–41
17. S.D. Beattie and J.R. Dahn, Comparison of Electrodeposited Copper-Zinc Alloys Prepared Individually and Combinatorially, *J. Electrochem. Soc.*, 2003, **150**(11), p C802–C806
18. S.S. Lee, T.H. Kim, J.S. Hu, W.W. Cai, J.A. Abell, and J. Li, Characterization of Joint Quality in Ultrasonic Welding of Battery Tabs, *J. Manuf. Sci. Eng.*, 2013, **135**(2), p 1–13
19. C.Q. Zhang, J.D. Robson, and P.B. Prangnell, Dissimilar Ultrasonic Spot Welding of Aerospace Aluminum Alloy AA2139 to Titanium Alloy TiAl6V4, *J. Mater. Process. Technol.*, 2016, **231**, p 382–388
20. C.Q. Zhang, J.D. Robson, O. Ciuca, and P.B. Prangnell, Microstructural Characterization and Mechanical Properties of High Power Ultrasonic Spot Welded Aluminum Alloy AA6111–TiAl6V4 Dissimilar Joints, *Mater. Charact.*, 2014, **97**, p 83–91
21. V.K. Patel, S.D. Bhole, and D.L. Chen, Ultrasonic Spot Welding of Aluminum to High-Strength Low-Alloy Steel: Microstructure, Tensile and Fatigue Properties, *Metall. Mater. Trans. A*, 2014, **45**(4), p 2055–2066
22. F. Haddadi, Rapid Intermetallic Growth Under High Strain Rate Deformation During High Power Ultrasonic Spot Welding of Aluminium to Steel, *Mater. Des.*, 2015, **66**, p 459–472
23. A. Macwan and D.L. Chen, Ultrasonic Spot Welding of Rare-Earth Containing ZEK100 Magnesium Alloy to 5754 Aluminum Alloy, *Mater. Sci. Eng. A*, 2016, **666**, p 139–148
24. M.-L. Zhu and F.-Z. Xuan, Effect of Microstructure on Strain Hardening and Strength Distributions Along a Cr–Ni–Mo–V Steel Welded Joint, *Mater. Des.*, 2015, **65**, p 707–715
25. D.-Q. Wang, M.-L. Zhu, and F.-Z. Xuan, Correlation of Local Strain with Microstructures Around Fusion Zone of a Cr–Ni–Mo–V Steel Welded Joint, *Mater. Sci. Eng. A*, 2017, **685**, p 205–212



26. M.-L. Zhu, F.-Z. Xuan, and J. Chen, Influence of Microstructure and Microdefects on Long-Term Fatigue Behavior of a Cr–Mo–V Steel, *Mater. Sci. Eng. A*, 2012, **546**, p 90–96
27. M.G. Nicholas and C.F. Old, Liquid Metal Embrittlement, *J. Mater. Sci.*, 1979, **14**(1), p 1–18
28. R.M. Bruscatto, Liquid Metal Embrittlement of Austenitic Stainless Steel When Welded to Galvanized Steel, *Weld. J. N. Y.*, 1992, **71**, p 455–460
29. C.Y. Zhang, D.L. Chen, and A.A. Luo, Joining 5754 Automotive Aluminum Alloy 2-mm-Thick Sheets Using Ultrasonic Spot Welding, *Weld. J.*, 2014, **93**, p 131–138
30. F. Haddadi, D. Strong, and P.B. Prangnell, Effect of Zinc Coatings on Joint Properties and Interfacial Reactions in Aluminum to Steel Ultrasonic Spot Welding, *JOM*, 2012, **64**(3), p 407–413
31. L. Xu, L. Wang, Y.-C. Chen, J.D. Robson, and P.B. Prangnell, Effect of Interfacial Reaction on the Mechanical Performance of Steel to Aluminum Dissimilar Ultrasonic Spot Welds, *Metall. Mater. Trans. A*, 2016, **47**(1), p 334–346
32. C.P. Wang, X.J. Liu, M. Jiang, I. Ohnuma, R. Kainuma, and K. Ishida, Thermodynamic Database of the Phase Diagrams in Copper Base Alloy Systems, *J. Phys. Chem. Solids*, 2005, **66**(2), p 256–260